Article

Resolving the H I in damped Lyman α systems that power star formation

https://doi.org/10.1038/s41586-022-04616-1

Received: 18 August 2021

Accepted: 4 March 2022

Published online: 18 May 2022

Check for updates

Rongmon Bordoloi[1✉], John M. O'Meara[2], Keren Sharon[3], Jane R. Rigby[4], Jeff Cooke[5,6], Ahmed Shaban[1], Mateusz Matuszewski[7], Luca Rizzi[2], Greg Doppmann[2], D. Christopher Martin[7], Anna M. Moore[8], Patrick Morrissey[7] & James D. Neill[7]

Reservoirs of dense atomic gas (primarily hydrogen) contain approximately 90 per cent of the neutral gas at a redshift of 3, and contribute to between 2 and 3 per cent of the total baryons in the Universe[1–4]. These 'damped Lyman α systems'—so called because they absorb Lyman α photons within and from background sources—have been studied for decades, but only through absorption lines present in the spectra of background quasars and γ-ray bursts[5–10]. Such pencil beams do not constrain the physical extent of the systems. Here we report integral-field spectroscopy of a bright, gravitationally lensed galaxy at a redshift of 2.7 with two foreground damped Lyman α systems. These systems are greater than 238 kiloparsecs squared in extent, with column densities of neutral hydrogen varying by more than an order of magnitude on scales of less than 3 kiloparsecs. The mean column densities are between $10^{20.46}$ and $10^{20.84}$ centimetres squared and the total masses are greater than 5.5×10^{8}–1.4×10^{9} times the mass of the Sun, showing that they contain the necessary fuel for the next generation of star formation, consistent with relatively massive, low-luminosity primeval galaxies at redshifts greater than 2.

We use the Keck Cosmic Web Imager (KCWI)[11] installed on the W. M. Keck Observatory to observe the gravitationally lensed arc SGAS J152745.1+065219 (SGAS, SDSS Giant Arcs Survey; SDSS, Sloan Digital Sky Survey). This arc is formed owing to strong gravitational lensing of a galaxy at $z \approx 2.762$, highly magnified and stretched by a massive galaxy cluster at $z \approx 0.392$[12]. Magellan/MagE echelle spectroscopy[13] of the brightest knot of this arc reveals the presence of multiple intervening absorption systems, including a redshift $z = 2.543$ system that shows C IV and damped Lyman α absorption (J.R.R., R.B. & J. Chisholm, unpublished data). We perform KCWI observations to spatially map out the damped Lyman α system (DLA) along the arc. The KCWI observations reveal the presence of a second DLA at $z \approx 2.05$, at a redshift where the MagE/Magellan observations detect intervening C IV absorption.

Figure 1 shows a spatial map of neutral hydrogen column density ($N_{\mathrm{H\,I}}$) in the $z \approx 2.5$ DLA. We extract moderate signal-to-noise ratio (SNR) spectra for six distinct, spatially resolved positions across the 7-arcsecond spatial extent of SGAS J152745.1+065219 (see Methods). These spectra facilitate a direct analysis of the spatial variation in $N_{\mathrm{H\,I}}$ and the amount of absorption by various heavy elements for the two DLAs along the six lines of sight. Spatially resolved maps of neutral hydrogen and heavy-element atomic transitions in high-redshift galaxies are highly complementary to lensing tomography of Mg II absorption at intermediate redshifts[14,15], quasar lens statistics[16,17] and spatially resolved studies of galactic outflows[18].

Several key features of the $z \approx 2.5$ DLA are immediately visible from Fig. 1: (a) strong damped hydrogen absorption is detected at every pointing along the arc; (b) $N_{\mathrm{H\,I}}$ varies monotonically by an order of magnitude ($\log N_{\mathrm{H\,I}} \approx 19.9$–$20.8\ \mathrm{cm^{-2}}$) along the east–west extent of the arc, corresponding to approximately 1 dex in $N_{\mathrm{H\,I}}$ column density variation over 2–3 kpc in the absorber source plane (see Methods); (c) the Lyman α feature trough reaches zero flux (except in aperture F), indicating total or nearly total coverage of the area illuminated by the background galaxy; and (d) the nonzero Lyman α absorption trough in aperture F with damping wings is indicative of partial DLA coverage, which itself helps add a limit to the DLA size.

Along with $N_{\mathrm{H\,I}}$ column density variation, we observe large variations in metal absorption line strengths within the $z \approx 2.5$ DLA. Figure 2 shows the variation in absorption strengths of $N_{\mathrm{H\,I}}$, neutral oxygen (O I) and ionized C IV in the source plane of the absorber. The O I absorption strengths along this DLA vary by almost a factor of two, with apertures B and D showing the highest absorption strengths and aperture F showing a non-detection. Different ionization states

---

[1]Department of Physics, North Carolina State University, Raleigh, NC, USA. [2]W.M. Keck Observatory, Kamuela, HI, USA. [3]Department of Astronomy, University of Michigan, Ann Arbor, MI, USA. [4]Observational Cosmology Lab, NASA Goddard Space Flight Center, Greenbelt, MD, USA. [5]Centre for Astrophysics and Supercomputing, Swinburne University of Technology, Hawthorn, Victoria, Australia. [6]The Australian Research Council Centre of Excellence for All Sky Astrophysics in 3 Dimensions (ASTRO-3D), Hawthorn, Victoria, Australia. [7]Cahill Center for Astrophysics, Caltech, Pasadena, CA, USA. [8]Research School of Astronomy and Astrophysics, Australian National University, Canberra, Australian Capital Territory, Australia.
✉e-mail: rbordol@ncsu.edu

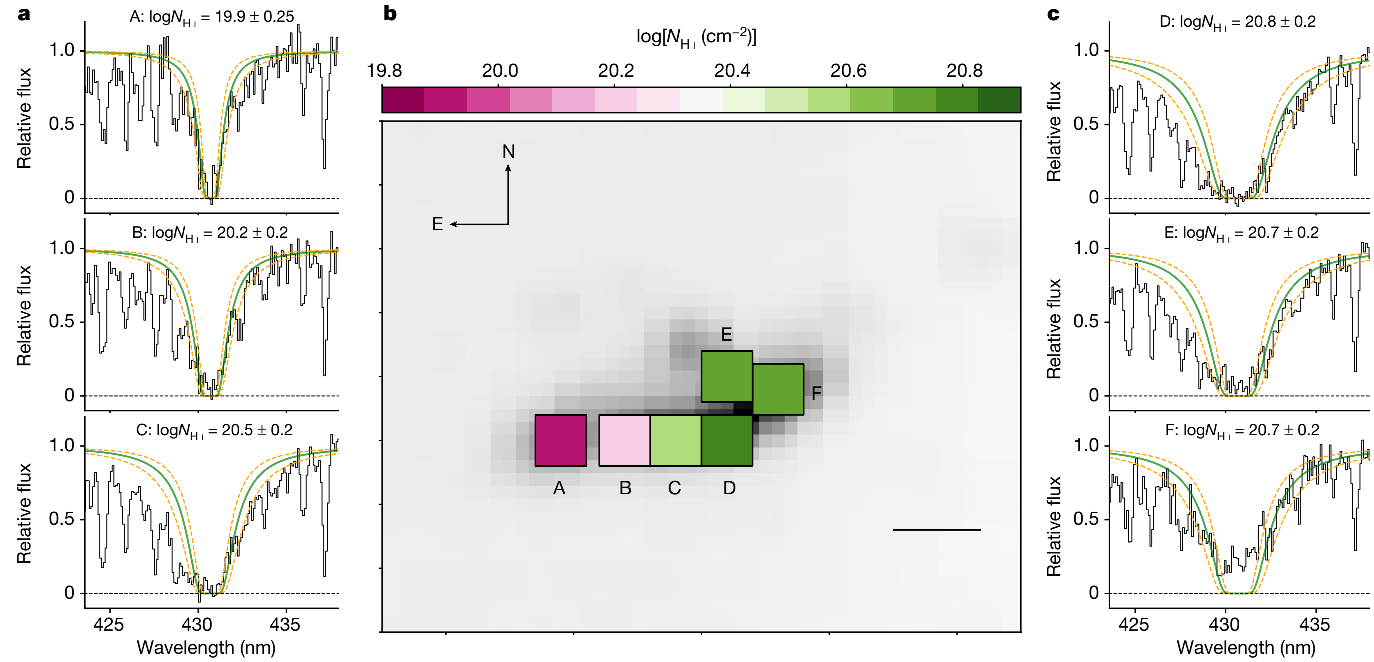

Fig. 1 | Spatial variation of neutral hydrogen column density. a, Extracted $z \approx 2.5$ DLA absorption and the Voigt profile fits used to constrain H I column densities for extraction boxes A–C. The DLA column densities noted in each panel are in units of atoms cm^{-2}. Errors quoted are $\pm 1\sigma$ uncertainties in column densities. **b**, Keck/KCWI white-light image of the background lensed galaxy at $z \approx 2.7$ is shown in grey. The filled squares mark the apertures used in 1D spectral extractions that are used to measure the absorption line properties. The squares are colour-coded by their neutral hydrogen column densities in units of atoms cm^{-2}. The scale bar corresponds to 2″ in the image plane. The extraction boxes are chosen in the image plane, which correspond to a spatial separation of approximately 2–3 kpc in the source plane of the absorber (see Methods). Over the approximately 2–3 kpc spatial separation, the DLA column densities vary by approximately 0.9 dex. **c**, Extracted $z \approx 2.5$ DLA absorption and the Voigt profile fits used to constrain H I column densities for extraction boxes D–F.

exhibit significantly different absorption within the same DLA system. The DLA shows large variation in both $N_{\mathrm{H\,I}}$ (average HI column density $\langle \log N_{\mathrm{H\,I}} \rangle \approx 20.46 \pm 0.32$ cm^{-2}) and metal absorption strengths and exceeds our conservative 1σ errors on the individual H I estimate of 0.2 dex (Extended Data Table 1). The DLA is extended along the declination direction by $\Delta\delta \gtrsim 15.9 \pm 1.4$ kpc and along right ascension by $\Delta\alpha \gtrsim 6.9 \pm 1.5$ kpc. Each extraction box samples areas of approximately 2–7 kpc^2 (depending on where the box lies relative to the regions of strongest magnification) at the redshift of the $z \approx 2.5$ DLA. Such continuous map of spatial variation in an individual DLA is not possible to observe with quasar lines-of-sight studies, because quasars are parsec-scale skewers and multiple quasars appearing sufficiently close together on the sky are extremely rare. The spatial scales probed in this work are similar in size to those probed by very-high-resolution simulations of galaxies and the circumgalactic medium[19], providing constraints on the small-scale structure and sizes of individual neutral and ionized CGM gas. These constraints can be used independently to test the subgrid feedback and star-formation prescriptions as well as physical models of gas inflow, outflow and recycling implemented in simulations[19,20].

The Lyman α troughs in most spectra are optically thick (that is, little to no by-passing flux), and so we can constrain the minimum size and mass of the DLA by estimating the size of the area covered by the six intervening lines of sight. Such fundamental quantities are largely unconstrained[21,22]. Aperture F is a particularly interesting sightline, as the damped absorption wings confirm it as a DLA, but the absorption trough shows substantial by-passing flux (greater than approximately 75% of aperture area covers the background galaxy). This is an example of partial coverage of a DLA in front of an extended background source and validates the technique of using extended background sources to assess DLA sizes via their partial $N_{\mathrm{H\,I}}$ coverage[22]. The maximum extent of the extraction aperture boxes in the six sightlines is $d = 17.4 \pm 0.6$ kpc, corresponding to a minimum projected area of greater than approximately 238 kpc^2, assuming a circular geometry. We stress that this estimate is a lower limit, as the DLA could extend farther than the area mapped by the background light of SGAS J152745.1+065219, but offers the appealing prospect that we are seeing the edge of at least part of the DLA in aperture F. The column density $\langle \log N_{\mathrm{H\,I}} \rangle \approx 20.46 \pm 0.32$ cm^{-2} from an average of the separate estimates provided by each extraction box and a circular uniform slab geometry yields a total neutral hydrogen gas mass of greater than approximately $5.5^{+0.6}_{-0.3} \times 10^{8} M_{\odot}$, where $M_{\odot}$ is the mass of the Sun. Again, this estimate is a strict lower limit for the same reasons as the estimate of the spatial extent and carries the same lensing model uncertainties.

Figure 2b shows the spatial variation of the second $z \approx 2.055$ DLA, in its source plane. This DLA has higher average H I column density ($\langle \log N_{\mathrm{H\,I}} \rangle \approx 20.84 \pm 0.02$ cm^{-2}) and shows much smaller $N_{\mathrm{H\,I}}$ variation as compared to the former DLA. The variation in metal line absorption strength across the DLA is also more uniform compared to the former, suggesting a larger size with more uniform gas distribution. None of the absorption troughs show signs of partial coverage for this DLA (see Methods). Adopting a circular geometry of the H I across the entire absorber (maximum extent of the apertures $d = 18.02 \pm 0.56$ kpc) yields a projected area of greater than approximately 255 kpc^2 at $z = 2.0556$ and a total neutral hydrogen gas mass of greater than about $1.4^{+1.5}_{-0.7} \times 10^{9} M_{\odot}$. We stress that these are strictly lower limits for this DLA.

In the local Universe, extended H I disks are typically seen around galaxies at scales of up to a few kiloparsecs[23], with a small population

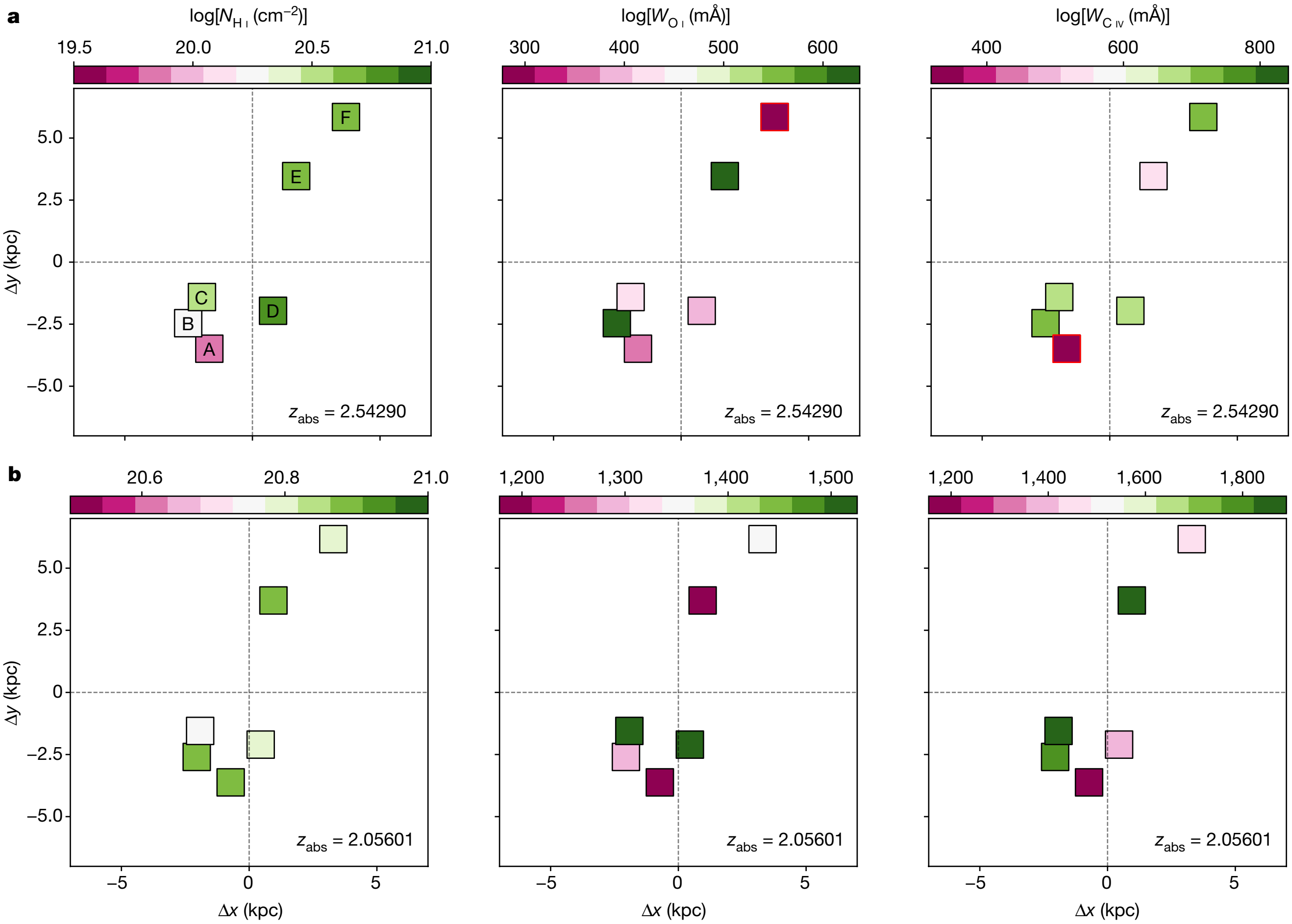

Fig. 2 | Maps of H I and metal absorption strengths in the absorber source-plane. a, Variation of the H I column density (left), O I absorption strength (middle) and C IV absorption strength (right) across the $z \approx 2.5$ DLA in its source plane. In each case, the filled squares are colour-coded as a function of their absorption strengths. The squares marked with red outlines are 2σ upper limits (see Extended Data Table 1). The squares are marked A–F to identify their location in the image plane (Fig. 1). **b**, As in **a**, but for the $z \approx 2.05$ DLA.

of disk galaxies showing extended H I disks out to tens of kiloparsecs[24]. It is also found that the H I kinematics in local H I disk galaxies[25] are two times smaller than typical DLA kinematics. Our results show that at $z > 2$, the two DLAs have a spatial extent greater than approximately 17 kpc, although the typical halo masses of disk galaxies are much larger at $z \approx 0$ as compared to at $z > 2$. This suggests that high-z DLAs might have sizes larger than the extended H I disks seen around local galaxies.

We further explore the two DLA systems by extracting a narrow region in wavelength from the KCWI cube corresponding to ±3.5 Å around the DLA line centre (see Methods). At these wavelengths, the DLA absorption line centre should absorb all the light from SGAS J152745.1+065219, if the optically thick DLA gas covers the background-galaxy light source completely. Yet, as seen in Fig. 3b, c, faint, extended emission is detected in the absorption troughs of both DLAs in a spectrum extracted from the aperture marked in Fig. 3a. This emission is particularly strong for the DLA at $z \approx 2.05$. Some of this emission may stem from the continuum flux by the $z \approx 0.4$ foreground galaxy to the north of SGAS J152745.1+065219. Two options remain for the remaining flux that is well separated from the foreground galaxy: either the DLA gas only partially covers the background ultraviolet light from the continuum of SGAS J152745.1+065219, or it is Lyman α emission originating from the galaxies associated with the DLAs. We favour the latter interpretation, as a weak emission feature is seen in each extraction box. Moreover, the emission is slightly spatially offset from the brightest background light from SGAS J152745.1+065219 and is seen as small blue clumps in a Hubble Space Telescope (HST)/F475W image at these positions (Fig. 3). Thus, we interpret the emission as faint Lyman α emission from star formation in the two galaxies that host the $z \approx 2.543$ and $z \approx 2.055$ DLAs, seen in absorption and magnified by the gravitational lensing.

Searches for DLA galaxies in emission have yielded few results[26], with the general DLA population shown to be only weakly star-forming[27]. Lyman α emission is also seen in the extracted DLA spectra themselves, offset by approximately −150 to 300 km s^{-1} of the DLA line centre (Methods). One possible explanation for the offset Lyman α is the association of the Lyman α emitting gas with inflowing material onto the DLA. Another possibility is that the DLA gas is rotating, with non-uniform star formation throughout. Higher-resolution observations with higher signal-to-noise ratio are needed to better constrain the nature of the putative DLA emission. Figure 4 shows the location of all pixels with $>3\sigma$ surface brightness levels ($>1.9 \times 10^{-17}$ erg cm^{-2} s^{-1} arcsec^{-2}) in the source plane of the two DLAs. For comparison, the six positions at which DLA absorption are measured are also shown. The absorption-line probes are at very close impact parameter to the DLA hosts, and the hosts have a size typical of a Lyman break galaxy at these redshifts[28,29].

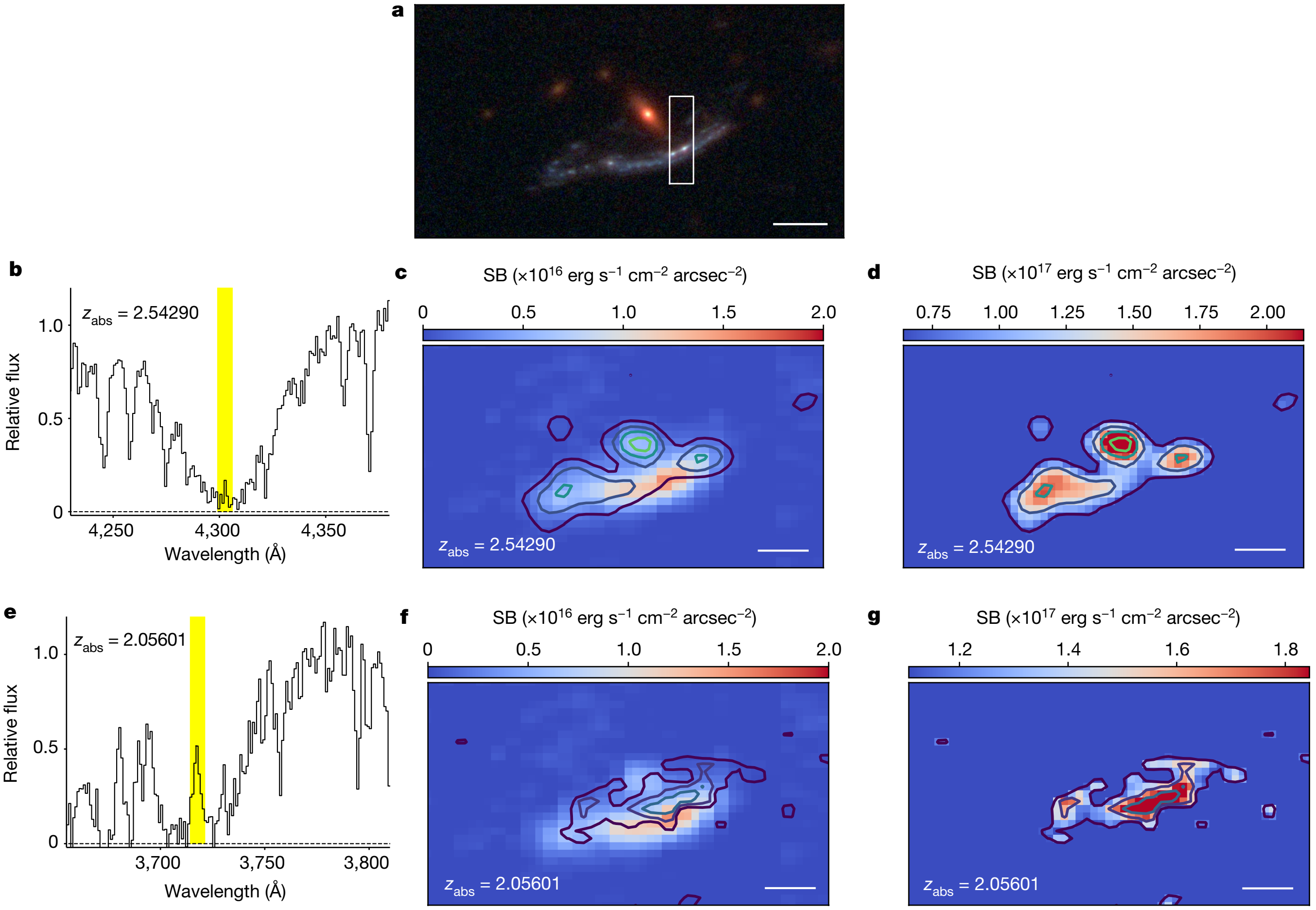

Fig. 3 | Lyman α emission maps of the DLA host galaxies. a, Colour image of the gravitationally lensed galaxy SGAS J152745.1+065219 rendered from HST/WFC3 F475W (blue), F606W (green) and F110W (red) filters. The rectangle marks the aperture from which extracted spectra are shown in **b** and **e**. Scale bar, 2″. **b**, Extracted 1D absorption profile of the foreground (z = 2.543) DLA. The yellow area marks the Lyman α emission seen in the 1D spectrum. **c**, Continuum emission from the background lensed galaxy (z = 2.762) in false colour, with contours marking the >3σ surface brightness (SB) levels of observed Lyman α emission from the foreground z = 2.543 DLA. **d**, Lyman α emission from the foreground z = 2.543 DLA (>3σ surface brightness levels; see Methods), obtained by summing the emission flux of the Keck/KCWI data cube around 1,212 Å ≤ λ ≤ 1,219 Å of the rest-frame wavelengths of the DLA. **e**–**g**, As in **b**–**d**, but for the foreground $z \approx$ 2.055 DLA. The Lyman α emission from the foreground DLAs are spatially offset from the background galaxy and extend out to at least the size of the background galaxy itself. Note that the surface brightness scales are different in the different panels. Scale bars, 2″.

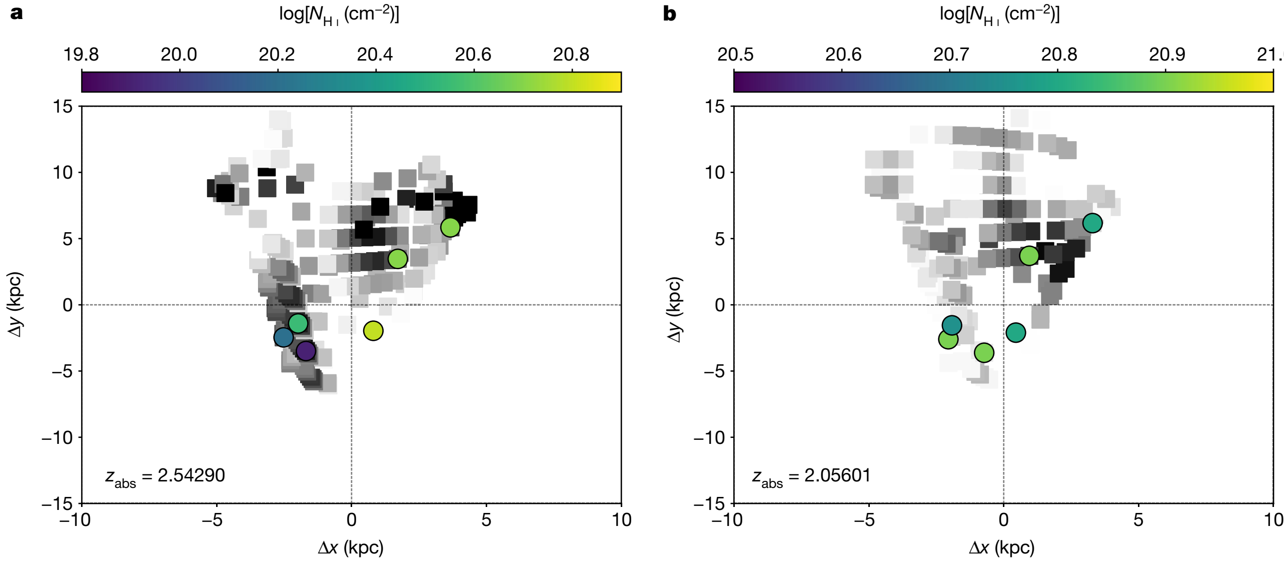

Fig. 4 | Lyman α emission from the background DLAs in their source planes. a, Source plane positions of pixels that show Lyman α emission with >3σ statistical significance in the rest frame of the $z \approx$ 2.5 DLA are shown. The filled circles show the DLA column density estimates obtained from absorption line spectroscopy (Fig. 1). The background lines of sight intersect the DLA host galaxy at very small (<1–2 kpc) impact parameter. **b**, As in **a**, but for the DLA at $z \approx$ 2.055. Lyman α emission from both of the DLA host galaxies have spatial extent similar to typical Lyman α emitters seen at these redshifts.

Online content

Any methods, additional references, Nature Research reporting summaries, source data, extended data, supplementary information, acknowledgements, peer review information; details of author contributions and competing interests; and statements of data and code availability are available at https://doi.org/10.1038/s41586-022-04616-1.

1. Weinberg, D. H., Miralda-Escude, J., Hernquist, L. & Katz, N. A lower bound on the cosmic baryon density. *Astrophys. J.* **490**, 564–570 (1997).
2. Cen, R. & Ostriker, J. P. Where are the baryons? *Astrophys. J.* **514**, 1–6 (1999).
3. Shull, J. M., Smith, B. D. & Danforth, C. W. The baryon census in a multiphase intergalactic medium: 30% of the baryons may still be missing. *Astrophys. J.* **759**, 23 (2012).
4. Péroux, C. & Howk, J. C. The cosmic baryon and metal cycles. *Annu. Rev. Astron. Astrophys.* **58**, 363–406 (2020).
5. Wolfe, A. M., Gawiser, E. & Prochaska, J. X. Damped Lyα systems. *Annu. Rev. Astron. Astrophys.* **43**, 861–918 (2005).
6. Neeleman, M. et al. [C II] 158-μm emission from the host galaxies of damped Lyman-alpha systems. *Science* **355**, 1285–1288 (2017).
7. Neeleman, M., Prochaska, J. X., Kanekar, N. & Rafelski, M. A cold, massive, rotating disk galaxy 1.5 billion years after the Big Bang. *Nature* **581**, 269–272 (2020).
8. Prochaska, J. X. et al. The UCSD/Keck damped Lyα abundance database: a decade of high-resolution spectroscopy. *Astrophys. J. Suppl. Ser.* **171**, 29–60 (2007).
9. Rafelski, M., Wolfe, A. M., Prochaska, J. X., Neeleman, M. & Mendez, A. J. Metallicity evolution of damped Lyα systems out to $z \sim 5$. *Astrophys. J.* **755**, 89 (2012).
10. Fox, A. J., Petitjean, P., Ledoux, C. & Srianand, R. Multiphase plasma in sub-damped Lyα systems: a hidden metal reservoir. *Astrophys. J. Lett.* **668**, L15–L18 (2007).
11. Morrissey, P. et al. The Keck Cosmic Web Imager Integral Field Spectrograph. *Astrophys. J.* **864**, 93 (2018).
12. Koester, B. P. et al. Two lensed $z \sim 3$ Lyman break galaxies discovered in the SDSS giant arcs survey. *Astrophys. J. Lett.* **723**, L73–L77 (2010).
13. Rigby, J. R. et al. The Magellan evolution of galaxies spectroscopic and ultraviolet reference atlas (MegaSaura). I. The sample and the spectra. *Astron. J* **155**, 104 (2018).
14. Lopez, S. et al. A clumpy and anisotropic galaxy halo at redshift 1 from gravitational-arc tomography. *Nature* **554**, 493–496 (2018).
15. Péroux, C., Rahmani, H., Battaia, F. & Augustin, R. Spatially resolved metal gas clouds. *Mon. Not. R. Astron. Soc.* **479**, L50–L54 (2018).
16. Rauch, M., Sargent, W., Barlow, T. & Simcoe, R. Small-scale structure at high redshift. IV. Low-ionization gas intersecting three lines of sight to Q2237+0305. *Astrophys. J.* **576**, 45–60 (2002).
17. Ellison, S. L. et al. The sizes and kinematic structure of absorption systems towards the lensed quasar APM08279+5255. *Astron. Astrophys.* **414**, 79–93 (2004).
18. Bordoloi, R. et al. Spatially resolved galactic wind in lensed galaxy RCSGA 032727-132609. *Mon. Not. R. Astron. Soc.* **458**, 1891–1908 (2016).
19. Peeples, M. S. et al. Figuring Out Gas & Galaxies in Enzo (FOGGIE). I. Resolving simulated circumgalactic absorption at $2 < z < 2.5$. *Astrophys. J.* **873**, 129 (2019).
20. Nelson, D. et al. First results from the TNG50 simulation: galactic outflows driven by supernovae and black hole feedback. *Mon. Not. R. Astron. Soc.* **490**, 3234–3261 (2019).
21. Mawatari, K. et al. Discovery of a damped Lyα absorber at $z = 3.3$ along a galaxy sight-line in the SSA22 field. *Astrophys. J.* **817**, 161 (2016).
22. Cooke, J. & O'Meara, J. M. A new constraint on the physical nature of damped Lyman alpha systems. *Astrophys. J. Lett.* **812**, L27 (2015).
23. Walter, F. et al. THINGS: The H I nearby galaxy survey. *Astron. J* **136**, 2563–2647 (2008).
24. Broeils, A. H. & van Woerden, H. A search for spiral galaxies with extended H I disks. *Astron. Astrophys. Suppl. Ser.* **107**, 129–176 (1994).
25. Zwaan, M. et al. Are the kinematics of DLAs in agreement with their arising in the gas disks of galaxies? *Astron. J* **136**, 2886–2896 (2008).
26. Krogager, J. K. et al. Dissecting cold gas in a high-redshift galaxy using a lensed background quasar. *Astron. Astrophys.* **619**, A142 (2018).
27. Fumagalli, M., O'Meara, J. M., Prochaska, J. X., Rafelski, M. & Kanekar, N. Directly imaging damped Lyα galaxies at $z > 2$ — III. The star formation rates of neutral gas reservoirs at $z \sim 2.7$. *Mon. Not. R. Astron. Soc.* **446**, 3178–3198 (2015).
28. Law, D. R. et al. The physical nature of rest-UV galaxy morphology during the peak epoch of galaxy formation. *Astrophys. J.* **656**, 1–26 (2007).
29. Law, D. et al. An HST/WFC3-IR morphological survey of galaxies at $z = 1.5–3.6$. I. Survey description and morphological properties of star-forming galaxies. *Astrophys. J.* **745**, 85 (2012).

Publisher's note Springer Nature remains neutral with regard to jurisdictional claims in published maps and institutional affiliations.

© The Author(s), under exclusive licence to Springer Nature Limited 2022

Methods

KCWI observations and data reduction

We observed SGAS J152745.1+065219 with KCWI for 2 h during the night of 2 June 2019. The instrument was configured with the Medium IFU slicer and the BL grating. This combination gives a 16.5″ × 20.4″ field of view, a slicer width of 0.69″, and a spectral resolution of $R \approx 2{,}000$. We obtained multiple exposures with exposure times between 600 and 1,800 seconds each. Between each exposure, the telescope was shifted by a few arcseconds in the east–west direction to facilitate sky subtraction. The raw data were processed using the publicly available kderp package (https://doi.org/10.5281/zenodo.1287322) developed by the KCWI team, which produces a wavelength- and flux-calibrated data cube for each exposure. Flux calibration was enabled by observing the flux standard Feige 67. We note that, unlike the HST data, KCWI does not have square pixels on the sky. To best facilitate visual comparison with the HST data (as is displayed in Figs. 1, 3), we resampled and optimally combined the KCWI data onto square pixels utilizing the Montage package[30]. Sky subtraction was performed globally on the cube by median sampling emission-free regions in the data at each wavelength and subtracting that median value from the image.

HST observations and lens model

SGAS J152745.1+065219 was observed by HST in Cycle 20 as part of the Sloan Giant Arcs Survey, GO-13003 (principal investigator, M. Gladders). All observations took place on UT 2013-01-16, with 1,211 s in WFC3/IR F160W, 1,111 s in WFC3/IR F110W, and 2,400 s each in WFC3/UVIS F606W and F475W. The data were reduced using the AstroDrizzle package[31], taking care to correct charge transfer efficiency (CTE) degradation effects, infrared blobs and other artefacts (a full description of the data reduction in this programme is available in previous papers)[32,33]. Images from the four filters were aligned to the same pixel frame of 0.03″ per pixel (Extended Data Fig. 1). The HST resolution and broad wavelength coverage enables detection of substructure in the main arc on very small spatial scales. SGAS J152745.1+065219 appears as three partial images of a background galaxy, each marked with a box in Extended Data Fig. 1. Owing to an alignment of this galaxy and the foreground lens, the central region of the galaxy is highly magnified and lensed into three images. The outskirts of the galaxy are not multiply-imaged and appear only once in the image plane.

The lens model is computed using the public software Lenstool[34] and described in detail in a previous publication[32]. The lensing potential in this sightline is dominated by a cluster of galaxies at redshift $z = 0.392$, as measured from spectroscopic redshifts of 14 cluster-member galaxies[35]. Moreover, KCWI spectroscopy of the field identifies at least three galaxies at $z \approx 0.43$. The lensed galaxy SGAS J152745.1+065219 that is the focus of this study is probably lensed by massive halos on multiple lens planes along the line of sight. Given the proximity of the lens planes, we compute the lens model by projecting the lenses onto the same plane.

The lensing potential of the cluster is constrained by multiple images of five background sources. After solving for the cluster mass distribution, we fix its parameters and treat the cluster as providing external shear when solving for the local lensing perturbation from the elliptical galaxy nearest to SGAS J152745.1+065219. The elliptical galaxy is parameterized as pseudo-isothermal ellipsoidal mass distribution[34], fixed to the position of the observed galaxy, and its ellipticity, position angle, cut radius, core radius and velocity dispersion are allowed to vary. The bright emission knots and the overall symmetry of SGAS J152745.1+065219 are used as constraints. The best set of parameters is identified in a Markov chain Monte Carlo process for both the cluster and galaxy halo. The source is reconstructed by ray-tracing the pixels from the HST image through the best-fit lens model, as can be seen in Extended Data Fig. 1b. One hundred Markov chain Monte Carlo posterior realizations are used to quantify the 1σ uncertainty in distances in the absorber planes.

Although the lensing geometry, multiplicity and distortion of SGAS J152745.1+065219 are a result of lensing from the nearby galaxy, the overall lensing potential in this sight line is dominated by the cluster. Unfortunately, the cluster itself is not well constrained. SGAS J152745.1+065219 is the brightest and most robust lensing constraint in this field, and the other lensed sources that were used to constrain the cluster lensing potential have not been spectroscopically confirmed. This increases the uncertainty on the model outputs[32]. As a result, we place a high uncertainty of a factor of two on the lensing magnification of SGAS J152745.1+065219, estimated from a range of models of the foreground cluster. Despite the high magnification uncertainty, the lensing geometry and multiplicity, as well as the source reconstruction, are all well understood.

Spectral extraction

We developed a custom spectral extraction pipeline to separate variable sized apertures from the KCWI cube (https://doi.org/10.5281/zenodo.6079396). There is an astrometric offset between the KCWI and HST astrometric solutions. We first offset the KCWI astrometric solution to match the HST observations by offsetting the KCWI astrometry by −0.24 arcsec along the right ascension and 1.8 arcsec along the declination directions, respectively. We then select six spatially separated regions on the KCWI white-light image (Fig. 1) to extract one-dimensional (1D) spectra from the KCWI data cube. Our choice of 5 × 5 spatial pixel box size is made to best balance the signal-to-noise ratio of the extracted spectrum and the desire for small spatial sampling across the SGAS J152745.1+065219 background source. The extracted aperture size exceeds the size of the full-width at half-maximum, FWHM ≈ 0.8″ seeing conditions during the observations with KCWI. For each extraction box, we perform a light-weighted optimal extraction by weighting each pixel of the extraction box by the white-light image of the data cube. This results in maximum signal-to-noise-ratio for the extracted 1D spectra.

Absorber modelling and physical characterization of the DLA gas

Because of the large wavelength extent of the absorption feature, the extracted KCWI spectra are of sufficient resolution and signal to noise to perform a Voigt profile analysis of the H I absorption. Using the linetools suite of routines (https://doi.org/10.5281/zenodo.168270), we place a single H I absorption line at $z = 2.543$ and at $z = 2.055$ and vary the H I content until an acceptable model to the data is obtained. Metal absorption lines associated with the two DLAs are single absorption component clouds, justifying the use of a single H I component in the fit. Continuum placement is chosen to match the flux of SGAS J152745.1+065219 on either side of the strong DLA absorption feature. The best fit H I value is obtained by performing chi-squared minimization using the Levenberg–Marquardt algorithm. The column density uncertainties presented are 1σ uncertainties on the model fit. In Fig. 1, we show the adopted fits on the six extraction boxes for the $z = 2.543$ DLA. Figure 2 and Extended Data Table 1 summarize these measurements.

As the background arc allows the sampling of the same foreground DLAs at different spatial locations, we can study the variation of DLA column density between individual sightlines. There are six unique extracted sightlines piercing the two foreground DLAs, yielding column density differences at 15 distinct physical separations between these sightlines per DLA. Extended Data Fig. 2 shows the $\log N_{\rm H\,I}$ variation between 15 separations for each DLAs in their source plane, respectively. It is particularly striking that for the $z = 2.543$ DLA (blue squares), the H I column density varies by an order of magnitude for every 2–3 kpc separation. This large variation suggests the presence of considerable small-scale variations within the DLA itself. These values are consistent with our aperture sampling sizes of approximately 2–7 kpc^2 in the source plane of the DLAs. Using broad emission line regions of quasi-stellar objects (QSOs) it has been shown that proximate DLA clouds near QSOs may be even smaller (<0.32 pc)[36]. However, the current data do not allow the mapping at these spatial scales owing to the trade-off between SNR and seeing. Future observations at either higher SNR, higher spatial resolution (that is, smaller KCWI slicer widths) or both would help explore these smaller scales. This specific example shows the DLA to be a gaseous structure with considerable small-scale variation in gas column density and demonstrates the power of this approach of combining IFU observations with gravitational lensing to gain unique insights into such systems.

The spectral resolution of the KCWI data is not sufficient to perform a similar Voigt profile analysis on the detected metal absorption lines. Instead, we measure the equivalent width of various ions and adopt the apparent optical depth (AOD) column densities for further analysis. We use a custom absorption line measurement pipeline (https://doi.org/10.5281/zenodo.6079264), optimized for CGM absorption line measurements. We perform a local continuum fit around each absorption line by fitting a fourth-order Legendre polynomial around ±1,000 km s^{-1} of each absorption line of interest. The 1σ uncertainty (σ_w) on each rest-frame equivalent width measurement is defined as $\sigma_w^2 = (\sum \sigma_\lambda^2 \Delta\lambda)/(1+z)$, where σ_λ is the 1σ normalized flux uncertainty per pixel, $\Delta\lambda$ is the wavelength difference between pixels and the summation is over the wavelength range of interest. An absorption line is defined as detected if its rest-frame equivalent width is $>3\sigma_w$. Extended Data Tables 1, 2 summarize these measurements.

Extended Data Fig. 3 shows the rest-frame equivalent width variations of O I 1302, Si II 1526, Si IV 1393, C II 1334 and C IV 1548 transitions as a function of projected physical separation from the centre of the background arc, respectively. In the $z \approx 2.5$ DLA (blue squares) the low ionization states (O I 1302) and high ionization states (Si IV 1393, C IV 1548) show non-detection in different apertures. The O I 1302 transition is not detected along aperture F (Fig. 2), which is the sightline with high H I column density, whereas both the Si IV and C IV transitions are not detected along aperture A, the sightline with the lowest H I column density. These variations suggest that the ionization conditions inside the DLA might also be varying.

In all cases the metal absorption line strengths in the $z \approx 2.5$ DLA (blue squares) are ~3–4 times weaker than those in the $z \approx 2.05$ DLA (red circles). The $z \approx 2.05$ DLA also exhibits much stronger H I column density than the former DLA. Extending the techniques demonstrated in this paper to a larger sample of spatially resolved DLAs will enable us to rigorously explore the hypothesis of whether low column density DLAs have much more small-scale variations than high column density systems in future works. As O I column densities are saturated in these low-resolution observations, we are not able to estimate accurate O I column densities and therefore cannot measure accurate DLA metallicities. Future works with higher SNR and resolution observations will enable the creation of metallicity maps at tens of parsec scale spatial resolution for this observation.

Spatially extended Lyman α emission

The extracted KCWI spectra at different spatial positions along the lensed arc show considerable variation in DLA column density (Fig. 2). However, when a 1D spectrum is extracted centred on the aperture shown in Fig. 3a, a faint emission spike is seen at the core of the DLA absorption for both the DLAs (Fig. 3b, e). The emission is particularly strong for the $z \approx 2.05$ DLA, and we detect strong emission spikes for all the apertures used in this study (Extended Data Fig. 4). We explore if this emission is seen on other parts of the sky by summing the flux around ±3.5 Å of Lyman α line centre at $z \approx 2.5$, and $z \approx 2.05$, respectively. Figure 3d, g shows the statistically significant ($>3\sigma$ surface brightness) Lyman α emission maps for both the DLAs, respectively. Note that the surface brightness colour bars show different scales for the two DLAs. Figure 3c, f shows the continuum image for the background lensed galaxy. The DLA Lyman α maps are overlaid in these panels as contours. The contours mark the 3σ to 15σ statistically significant surface brightness levels of Lyman α emission of both the DLAs, respectively. Some emission might come from the foreground cluster galaxy at $z \approx 0.4$, but the extended emission features on either side are not coming from this galaxy. Some of the diffuse emission features may be associated with the blue diffuse emission in the colour composite HST image (Fig. 3). The corresponding continuum emission from the background lensed galaxy SGAS J152745.1+065219 at $z \approx 2.7$ is shown in Fig. 3c, f. It is clearly seen that the Lyman α emission associated with the foreground DLA (contours) and the background lensed galaxy are not co-spatial. As we do not currently detect the continuum associated with this DLA Lyman α emission, we constrain the minimum Lyman α rest-frame emission equivalent width to be >1.1 Å for the $z \approx 2.5$ DLA, and >3.5 Å for the $z \approx 2.05$ DLA. These emission fluxes correspond to limits on host galaxy star-formation rates $>0.35 M_\odot$ yr^{-1} for the $z \approx 2.5$ DLA, and $>1\,M_\odot$ yr^{-1} for the $z \approx 2.05$ DLA.

Data availability

Data that support the findings of this study are publicly available at the Keck Observatory Archive, https://www2.keck.hawaii.edu/koa/public/koa.php, under project codes N083 and K338 and the Barbara A. Mikulski Archive for Space Telescope under project code GO-13003. Fully reduced data are available from the corresponding author upon request.

Code availability

All codes used in this work are publicly available. The H I column density measurements were performed using the linetools package (https://doi.org/10.5281/zenodo.168270). Reduction and analysis of the KCWI data cubes were done using the kcwitools package (https://doi.org/10.5281/zenodo.6079396). The lensing raytracing and absorption line measurements are done using the rbcodes package (https://doi.org/10.5281/zenodo.6079264). HST image analysis and lens modelling were performed with AstroDizzle[31] software and Lenstool[34], respectively.

30. Jacob, J. C. et al. Montage: an astronomical image mosaicking toolkit. Astrophysics Source Code Library https://www.ascl.net/1010.036 (2010).
31. Avila, R. J. et al. in *Astronomical Data Analysis Software and Systems XXIV (ADASS XXIV)* (eds Taylor, A. R. & Rosolowsky, E.) 281–284 (Astronomical Society of the Pacific, 2015).
32. Sharon, K. et al. Strong lens models for 37 clusters of galaxies from the SDSS giant arcs survey. *Astrophys. J. Suppl. Ser.* **247**, 12 (2020).
33. Sharon, K. & Johnson, T. L. Revised lens model for the multiply imaged lensed supernova, 'SN Refsdal' in MACS J1149+2223. *Astrophys. J. Lett.* **800**, L26 (2015).
34. Jullo, E. et al. A Bayesian approach to strong lensing modelling of galaxy clusters. *New J. Phys.* **9**, 447 (2007).
35. Bayliss, M. B. et al. Gemini/GMOS spectroscopy of 26 strong-lensing-selected galaxy cluster cores. *Astrophys. J. Suppl. Ser.* **193**, 8 (2011).
36. Fathivavsari, H. et al. A ghostly damped Ly α system revealed by metal absorption lines. *Mon. Not. R. Astron. Soc.* **466**, L58–L62 (2017).

Acknowledgements This work was supported by a NASA Keck PI Data Award, administered by the NASA Exoplanet Science Institute. Data presented herein were obtained at the W. M. Keck Observatory from telescope time allocated to the National Aeronautics and Space Administration (NASA) through the agency's scientific partnership with the California Institute of Technology and the University of California. The Observatory was made possible by the generous financial support of the W. M. Keck Foundation. This research was conducted, in part, by the Australian Research Council Centre of Excellence for All Sky Astrophysics in 3 Dimensions (ASTRO 3D), through project number CE170100013. We wish to recognize and acknowledge the very significant cultural role and reverence that the summit of Mauna Kea has always had within the indigenous Hawaiian community. We are most fortunate to have the opportunity to conduct observations from this mountain. This research made use of Montage. It is funded by the National Science Foundation under grant number ACI-1440620, and was previously funded by the NASA's Earth Science Technology Office, Computation Technologies Project, under cooperative agreement number NCC5-626 between NASA and the California Institute of Technology.

Author contributions R.B. and J.M.O. developed the idea for the project, wrote the NASA/Keck telescope proposal and designed and performed the observations. R.B. developed the analysis tools, performed the analysis, devised original ways to interpret the results and authored majority of the text. J.M.O. reduced the KCWI data. A.S. performed the metal absorption line measurements. K.S. performed the lens model and provided Extended Data Fig. 1. J.R.R. provided the ancillary data from MagE and metal absorber information from MagE spectra. J.C., J.M.O. and R.B. provided steps to correct astrometric offsets and J.C. confirmed the redshift of the second DLA, and contributed to the interpretations. M.M., L.R., G.D., D.C.M., A.M.M., P.M. and J.D.N. developed the KCWI data reduction pipeline and built and delivered the instrument when initial commissioning data provided the data needed to verify the target as an object of interest. All authors, including J.M.O., J.R.R. and J.C., contributed to the overall interpretation of the results and various aspects of the analysis and writing.

Competing interests The authors declare no competing interests.

Additional information

Correspondence and requests for materials should be addressed to Rongmon Bordoloi.

Peer review information *Nature* thanks Zachary Hafen and Marcel Neeleman for their contribution to the peer review of this work.

Reprints and permissions information is available at http://www.nature.com/reprints.

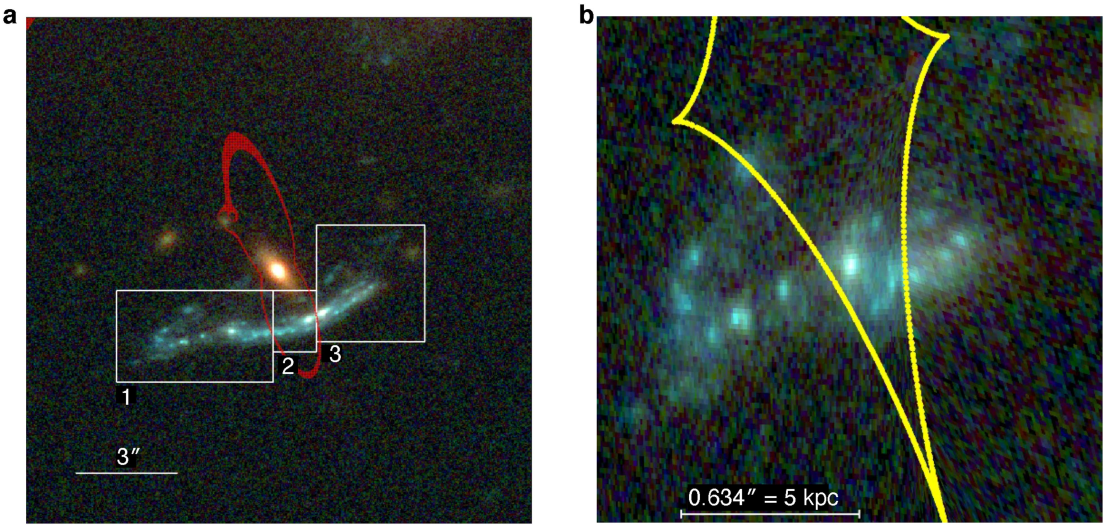

Extended Data Fig. 1 | Source plane reconstruction of SGAS J152745.1+065219. a, WFC3/HST images of SGAS J152745.1+065219 in the WFC3-IR F160W, WFC3-UVIS F606W and WFC3-UVIS F475W filters[32]. North is up and east is to the left. The gravitational lensing critical curve is shown in red, representing areas in the image plane with extreme magnification. Three boxes mark the locations of the three partially lensed images. The lensing potential is caused by the $z = 0.43$ elliptical galaxy at the centre of this field, boosted by a cluster of galaxies at $z = 0.39$, located within 1 arcminute in projection northeast of this galaxy. **b**, The reconstructed source plane image of the galaxy. The source-plane caustic is marked in yellow, representing regions with extreme magnification, and defining the multiplicity of the strongly lensed source. The region interior to the cusp is lensed into three images, whereas areas outside the cusp are magnified, but not multiply imaged.

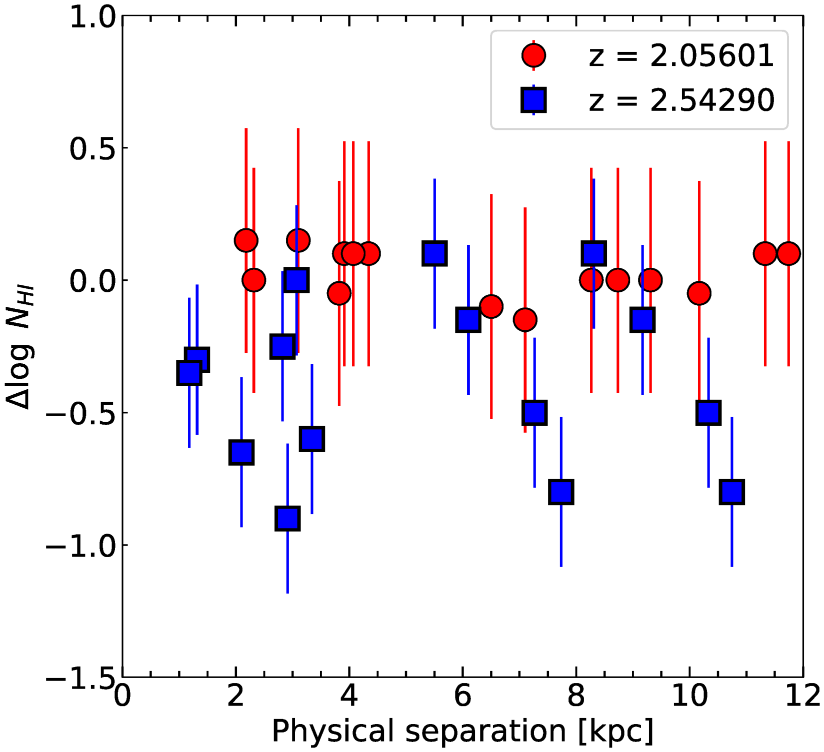

Extended Data Fig. 2 | Pairwise H i column density variation versus physical separation. Variation in H i column density between six individual pointings to the background arc as a function of physical separation between them. Error bars correspond to the ±1σ uncertainty in column density ratios. The $z \approx 2.5$ DLA (blue squares) shows an order-of-magnitude variation in column density in 2–3 kpc separations. This suggests significant small-scale variation inside the DLA, at 2–3 kpc physical scales. By contrast, the $z \approx 2.05$ DLA (red circles) shows very little variation in column densities across different sightlines. The red circles are offset in the x direction by 1 kpc for clarity of presentation.

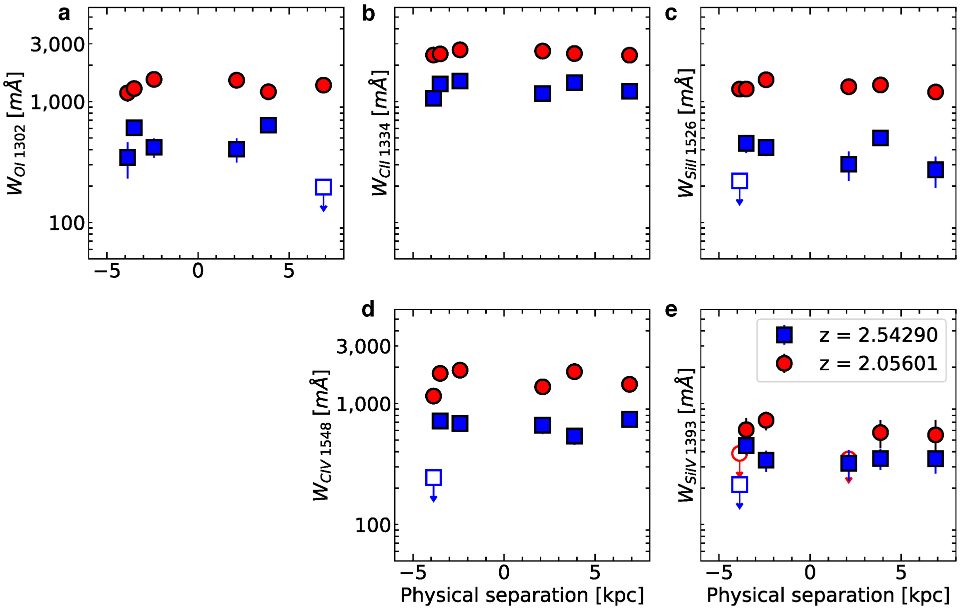

Extended Data Fig. 3 | Variation in metal absorption line strengths of the two DLA systems. a–e, Metal absorption line strength variations of different ions across the arc for the $z \approx 2.5$ DLA (blue squares) and the $z \approx 2.05$ DLA (red circles), respectively. The physical separations are in the source-plane of the absorbers and centred on the centre of the background arc. The filled symbols are detections, and the open symbols are 2σ limits of non-detections. Error bars correspond to the $\pm1\sigma$ uncertainty measurement of absorption strengths. In all cases, the $z \approx 2.5$ DLA exhibits much weaker metal absorption lines as compared to the $z \approx 2.05$ DLA.

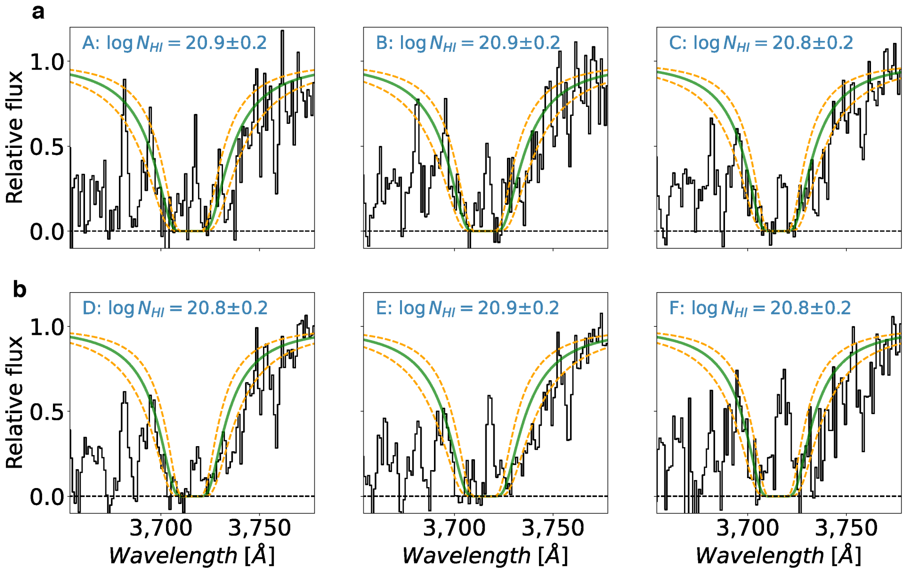

Extended Data Fig. 4 | Spatial variation of neutral hydrogen column density of the $z \approx 2.05$ DLA. a, The extracted 1D Lyman α absorption profiles are shown for apertures A–C. The best-fit Voigt profiles with ±1σ error bounds are shown as solid green and dashed orange lines, respectively. The DLA column densities are marked in each panel and are in units of atoms cm^{-2}. In each absorption profile, the DLA absorption trough reaches zero flux, indicating that the aperture is fully covering the DLA gas cloud. The emission spike in the middle of the absorption trough corresponds to Lyman α emission leaking out of the corresponding DLA host galaxy. **b**, As in **a**, but for apertures D–F.

Extended Data Table 1 | Absorption line measurements for the *z* = 2.54290 DLA

Aperture[a]	log N_{HI}[b]	W_{OI1302}[c]	$W_{CII1334}$[c]	$W_{SiII1526}$[c]	$W_{CIV1548}$[c]	$W_{SiIV1393}$[c]
A	19.90 ± 0.2	345 ± 114	1062 ± 120	< 221	< 244	< 214
B	20.20 ± 0.2	607 ± 69	1400 ± 72	452 ± 77	720 ± 89	450 ± 73
C	20.55 ± 0.2	419 ± 76	1478 ± 65	418 ± 63	684 ± 79	341 ± 67
D	20.80 ± 0.2	404 ± 90	1164 ± 93	303 ± 81	663 ± 104	321 ± 92
E	20.70 ± 0.2	637 ± 74	1435 ± 73	499 ± 71	540 ± 85	351 ± 68
F	20.70 ± 0.2	< 196	1217 ± 88	272 ± 78	741 ± 104	350 ± 85

[a] Aperture name as denoted in Fig. 1. [b] Measured H I column densities from Voigt profile fitting. Errors are ±1σ uncertainties on column densities. [c] Rest-frame equivalent widths of different metal absorption lines in units of mÅ. Errors are ±1σ uncertainties on equivalent widths. The < signs denote 2σ non-detection limits.

Extended Data Table 2 | Absorption line measurements for the $z=2.05601$ DLA

Aperture[a]	log N_{HI}[b]	W_{OI1302}[c]	$W_{CII1334}$[c]	$W_{SiII1526}$[c]	$W_{CIV1548}$[c]	$W_{SiIV1393}$[c]
A	20.90 ± 0.3	1178 ± 181	2425 ± 257	1268 ± 123	1154 ± 131	< 387
B	20.90 ± 0.3	1280 ± 114	2478 ± 168	1269 ± 77	1778 ± 97	609 ± 150
C	20.75 ± 0.3	1525 ± 101	2677 ± 151	1515 ± 82	1890 ± 91	728 ± 127
D	20.80 ± 0.3	1501 ± 157	2615 ± 214	1327 ± 100	1376 ± 127	< 349
E	20.90 ± 0.3	1206 ± 96	2496 ± 166	1372 ± 85	1836 ± 99	577 ± 150
F	20.80 ± 0.3	1367 ± 153	2418 ± 223	1200 ± 110	1444 ± 124	551 ± 180

[a] Aperture name as denoted in Fig. 1. [b] Measured H I column densities from Voigt profile fitting. Errors are ±1σ uncertainties on column densities. [c] Rest-frame equivalent widths of different metal absorption lines in units of mÅ. Errors are ±1σ uncertainties on equivalent widths. The < signs denote 2σ non-detection limits.